




Synthesis, characterization, and single-crystal growth of a high-entropy rare-earth pyrochlore oxide

Candice Kinsler-Fedon ^{1,*} Qiang Zheng,^{1,2} Qing Huang,³ Eun Sang Choi,⁴ Jiaqiang Yan ² Haidong Zhou,³ David Mandrus,^{1,2} and Veerle Keppens ^{1,†}

¹*Department of Materials Science and Engineering, The University of Tennessee, Knoxville, Tennessee 37996, USA*

²*Materials Science and Technology Division, Oak Ridge National Laboratory, Oak Ridge, Tennessee 37831, USA*

³*Department of Physics and Astronomy, The University of Tennessee, Knoxville, Tennessee 37996, USA*

⁴*National High Magnetic Field Laboratory, Florida State University, Tallahassee, Florida 32310-3706, USA*



(Received 20 May 2020; accepted 10 September 2020; published 19 October 2020)

The synthesis and single-crystal growth of a rare-earth high-entropy oxide $(\text{Yb}_{0.2}\text{Tb}_{0.2}\text{Gd}_{0.2}\text{Dy}_{0.2}\text{Er}_{0.2})_2\text{Ti}_2\text{O}_7$ in the cubic pyrochlore phase $Fd\bar{3}m$ are achieved by solid-state reaction and optical floating-zone growth techniques. X-ray diffraction and a structure refinement analysis confirm a single-phase pyrochlore structure and lattice parameter of $a = 10.1152(3)$ Å. Additional characterization techniques, including scanning transmission electron microscopy and nanoscale electron-energy loss spectroscopy mapping, support a single-phase pyrochlore structure with a homogeneous mixture down to ~ 2.3 nm. Magnetization measurements on a single crystal reveal antiferromagnetic correlations with a spin-glass ground state. These results show that it is possible to grow large single crystals of a high entropy pyrochlore oxide, expanding the avenues for future high-entropy oxide research.

DOI: [10.1103/PhysRevMaterials.4.104411](https://doi.org/10.1103/PhysRevMaterials.4.104411)

I. INTRODUCTION

High-entropy oxides (HEOs), also referred to as configurationally complex oxides (CCOs), have attracted attention due to their tunability of multiple cations on a single site [1–16]. Following the concept of high-entropy alloys (HEAs), HEOs refer to oxides with multiple ions (five or more) on a single site [17,18]. Since the introduction in 2015 of HEOs stabilized in the rocksalt phase [1], the high-entropy concept has been expanded to various structures, including the rocksalt [1–3], fluorite [4,5], perovskite [6–9], spinel [10,11], and a rare-earth disilicate with monoclinic symmetry [12]. Novel functionalities have been discovered for these configurationally complex materials, including low thermal conductivity, high corrosion and oxidation resistance, increased electrical storage capacities, and lithium superionic conductivity at room temperature, to name a few [2,12–16]. Recent studies have given a comprehensive examination of HEOs and their magnetic properties, discussing new findings such as a long-range antiferromagnetic ground state in an HEO rocksalt, antiferromagnetic overall behavior in B-site HEO perovskites, and magnetic ordering variation in HEO spinels [3,8,11]. Until now, HEOs with the pyrochlore structure have not been widely examined and have been primarily published for high-entropy rare-earth zirconate polycrystals and powders [15,16].

Rare-earth pyrochlore oxides ($\text{A}_2\text{B}_2\text{O}_7$) have been studied extensively since the 1960s and are known to display a vast array of interesting properties [19–39]. Some of these topics include exotic magnetism at low temperatures, strong

irradiation amorphization resistance, tunable mechanical and thermal properties based on A and B cation radii, low thermal conductivity, high-pressure effects, and the role of defects [19–28]. Due to their geometric frustration, many of the single-component rare-earth titanates exhibit spin liquid, spin ice, or other unconventional long-range ordered ground states at low temperatures [29–31].

Adding multiple rare-earth cations to the geometrically frustrated sublattice site of the pyrochlore structure could potentially lead to new magnetic behavior given the complexity of the interactions. This report discusses the successful synthesis of $(\text{Yb}_{0.2}\text{Tb}_{0.2}\text{Gd}_{0.2}\text{Dy}_{0.2}\text{Er}_{0.2})_2\text{Ti}_2\text{O}_7$ or $(5\text{RE}_{0.2})_2\text{Ti}_2\text{O}_7$ HEO pyrochlore, its single-crystal growth using the optical floating-zone technique, and characterization of its structure and magnetic properties, identifying nanoscale-level mixed occupation of the rare-earth cations in the pyrochlore phase and significant evidence of an exotic magnetic ground state. Configurational entropy was chosen for the A site of the $\text{RE}_2\text{Ti}_2\text{O}_7$ system, because each rare-earth cation forms a pyrochlore in its single-component (binary) form, obeying the A-site to B-site cation ratio rule (1.36–1.78 Å, roughly) needed to form the (227) structure [29,32]. All five rare-earth cations are magnetic, and configurational entropy on this sublattice is expected to be a good starting point for discovering novel materials with possible spin-glass or spin liquid ground states.

II. EXPERIMENTAL PROCEDURE

Solid-state reaction was used to form a single-phase polycrystalline $(5\text{RE}_{0.2})_2\text{Ti}_2\text{O}_7$. Starting reactants were Yb_2O_3 (99.9%), Tb_2O_3 (99.9%), Gd_2O_3 (99.9%), Dy_2O_3 (99.9%), Er_2O_3 (99.9%), and TiO_2 (99.9%). The rare-earth oxide

*Corresponding author: ckinsle1@vols.utk.edu

†Corresponding author: vkeppens@utk.edu

starting components were dried overnight at 1073 K in air. The dried powders were weighed at room temperature, combined, and mixed using a vibratory ball mill (SPEX 8000M Mixer/Mill) in a polypropylene grinding vial with two 12.7-mm methacrylate mixing balls for over an hour. The powder was pressed into a pellet, which was heated in a high-temperature box furnace at 1673 K for 20 h in air. The powders were removed, the x-ray diffraction pattern was checked, and the pellet reheated for another 20-h heat treatment. This process was repeated (approximately 3–4 times) until a single-phase x-ray diffraction pattern was observed.

Single crystals were grown using the floating-zone crystal growth technique with a two-mirror optical floating-zone furnace (Canon Machinery model SC1-MDH) and 1500-W halogen lamps. The single-phase powder was put into a balloon sleeve and pressed into a long rod pellet using a water cell press. The rod was heated at 1673 K for 20 h and prepared for single-crystal growth by cutting it into two unequal-length pieces (feed and seed rods). A hole was made at one end of the feed rod for a platinum wire to be fed through for hanging inside the quartz chamber. The seed rod was fastened to the bottom of the chamber accordingly. Growing conditions for the $(5RE_{0.2})_2Ti_2O_7$ crystal growth consisted of an oxygen atmosphere at a pressure of 0.3 MPa and a growth rate of 15–20 mm per hour. The rods were counter-rotated at 20–25 rpm. Crystal quality was determined by Laue diffraction using a Huber x-ray diffractometer and HD-CR 35 NDT for digital imaging of the crystal structure.

The room-temperature crystal structure was determined by x-ray diffraction using a PANalytical Empyrean multipurpose diffractometer (Cu $K\alpha_1$ radiation). A structure refinement analysis was performed using the General Structure Analysis System II (GSAS-II) software [40] to determine the crystallographic parameters of the HEO pyrochlore. Microscopy of the sample surface was performed using a Zeiss EVO scanning electron microscope with Bruker xFlash 6130 energy-dispersive x-ray spectrometer (EDXS).

Scanning transmission electron microscopy (STEM) measurements were conducted for further confirmation of a single-phase structure and homogeneous distribution of the rare-earth cations. Single-crystalline and polycrystalline $(5RE_{0.2})_2Ti_2O_7$ were crushed in ethanol. Drops of the resulting suspensions were deposited on lacey carbon TEM grids and dried in air for STEM observations. High-angle annular dark-field (HAADF) imaging and electron-energy loss spectroscopy (EELS) were performed on a Nion UltraSTEM100 equipped with a cold field-emission gun and a corrector of third- and fifth-order aberrations, operated at an accelerating voltage of 100 kV. HAADF-STEM images were collected with a probe convergence angle of 30 mrad and an inner collection angle of 86 mrad. EEL spectra were collected using a Gatan Enfium spectrometer (Gatan Inc.) with a dispersion of 0.5 eV per channel and collection semiangle of 48 mrad.

A superconducting interference device magnetometer (Quantum Design MPMS) was employed for the DC susceptibility measurements for the polycrystalline and single-crystal samples with an applied magnetic field of 1000 Oe and data taken from 3 to 300 K. For the single crystal, the DC susceptibility was measured with the field parallel to the [100] direction. Magnetization versus field (M vs H)

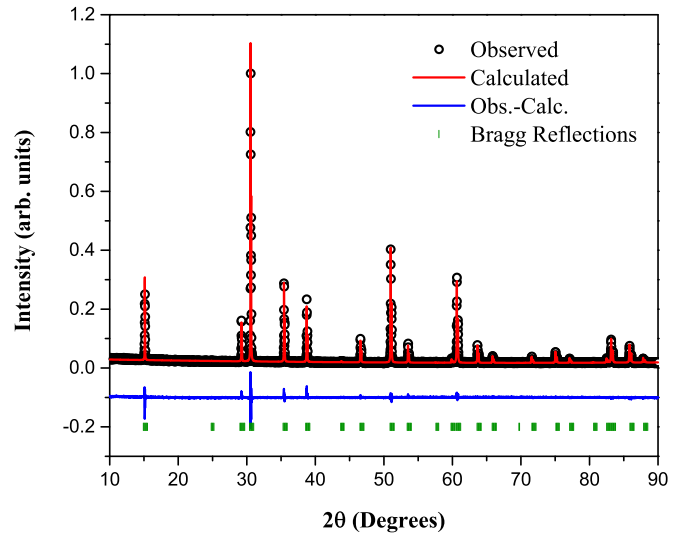


FIG. 1. Room-temperature powder x-ray diffraction pattern of polycrystalline $(5RE_{0.2})_2Ti_2O_7$. The refinement pattern (red line) overlays the observed pattern (black circles) which matches the $Fd\bar{3}m$ cubic structure (green vertical dashed lines are the Bragg reflections characteristic of the pyrochlore phase). The difference pattern is represented in blue below the diffraction pattern.

measurements were recorded using magnetic fields up to 7 T. Low-temperature (0.3–1.7 K) AC susceptibility measurements were performed at the National High Magnetic Field Laboratory with frequencies ranging from 47 to 995 Hz and magnetic fields up to 1 T.

III. RESULTS AND DISCUSSION

A. Structure and x-ray diffraction for polycrystalline $(5RE_{0.2})_2Ti_2O_7$

X-ray diffraction data and structure refinement recorded for polycrystalline $(5RE_{0.2})_2Ti_2O_7$ (Fig. 1) show that the multicomponent oxide has a cubic structure and belongs to the $Fd\bar{3}m$ space group. The diffraction pattern matches closely with the patterns of the standard cubic pyrochlore rare-earth titanates. Results of the structure refinement, including refined crystallographic parameters and powder x-ray diffraction data, are listed in the Supplemental [41].

The lattice parameter was found to be 10.1152(3) Å for $(5RE_{0.2})_2Ti_2O_7$, which is comparable to the single rare-earth component titanate pyrochlores from literature [34–38] listed in Table I. The lattice parameter for $(5RE_{0.2})_2Ti_2O_7$ falls in between the lattice parameters of $Yb_2Ti_2O_7$ and $Dy_2Ti_2O_7$, consistent with an even proportion of each rare-earth ion on the rare-earth site of $(5RE_{0.2})_2Ti_2O_7$. This result is expected, given that the average ionic radius is ~ 1.0218 Å for the five rare-earth cations, which falls between Dy^{3+} (1.027 Å) and Yb^{3+} (0.985 Å). The final refinement results, which include setting values to the instrument parameters (U , V , W) and refining the instrument parameter “ X ” to improve the reflection intensities, are very reasonable with values of $wRp = 6.34\%$, $R_{exp} = 4.38\%$, and the goodness of fit $\chi^2 = 1.45$.

TABLE I. List of comparable lattice parameters of the single-component rare-earth pyrochlore titanate oxides and HEO rare-earth pyrochlore titanate.

Rare-earth titanate pyrochlore compounds	Lattice parameter (Å)	Reference
$\text{Yb}_2\text{Ti}_2\text{O}_7$	10.09	[34]
$\text{Tb}_2\text{Ti}_2\text{O}_7$	10.158	[35]
$\text{Dy}_2\text{Ti}_2\text{O}_7$	10.131	[36]
$\text{Er}_2\text{Ti}_2\text{O}_7$	10.086	[37]
$\text{Gd}_2\text{Ti}_2\text{O}_7$	10.184	[38]
$(\text{Yb}_{0.2}\text{Tb}_{0.2}\text{Gd}_{0.2}\text{Dy}_{0.2}\text{Er}_{0.2})_2\text{Ti}_2\text{O}_7$	10.1152(3)	

B. Floating-zone crystal growth

Single-crystalline $(5RE_{0.2})_2\text{Ti}_2\text{O}_7$ was grown using the floating-zone growth technique with growing conditions as described in the Experimental Procedure. Figure 2(a) shows the resulting ingot of the single-crystal growth approximately 7 cm in length. The ingot has a brownish red color and is translucent. X-ray diffraction verified that the multicrystal was of the cubic pyrochlore phase, confirming that it did not change phase during growth (Fig. S3 in the SM [41]). Laue diffraction was used to determine crystal quality [Figs. 2(b)–2(d)] and indicates that the ingot contained multiple crystals of good quality ranging in size from 4 mm to 2 cm.

A former study of growing the single-component rare-earth titanate oxides using the same crystal growth technique reported success with slower growth rates ranging from 2.5 to 4 mm per hour [39]; however, these rates were not successful for the HEO rare-earth pyrochlore. Multiple attempts to

produce a completely single-domain crystal by using slower growth speeds ranging from 2 to 10 mm per hour resulted in unstable growth environments with bubble pocket formation or detachment of the molten zone. Adjusting the pressure from 0.3 to 0.2 MPa and pulling the crystal through the heated zone twice also had no improvement on the quality of the crystal. Having multiple rare-earth oxides with varying melting temperatures could be responsible for the crystal growth instability at slower speeds. Growing the crystal at a rate between 15 and 20 mm per hour was chosen as the growth speed range and produced a more stable growth overall. Improvements on the growth technique to obtain a larger high-quality single crystal will need further experimentation.

C. Microscopy and microstructure

Scanning electron microscopy (SEM) and energy-dispersive x-ray (EDX) analyses were conducted on both the

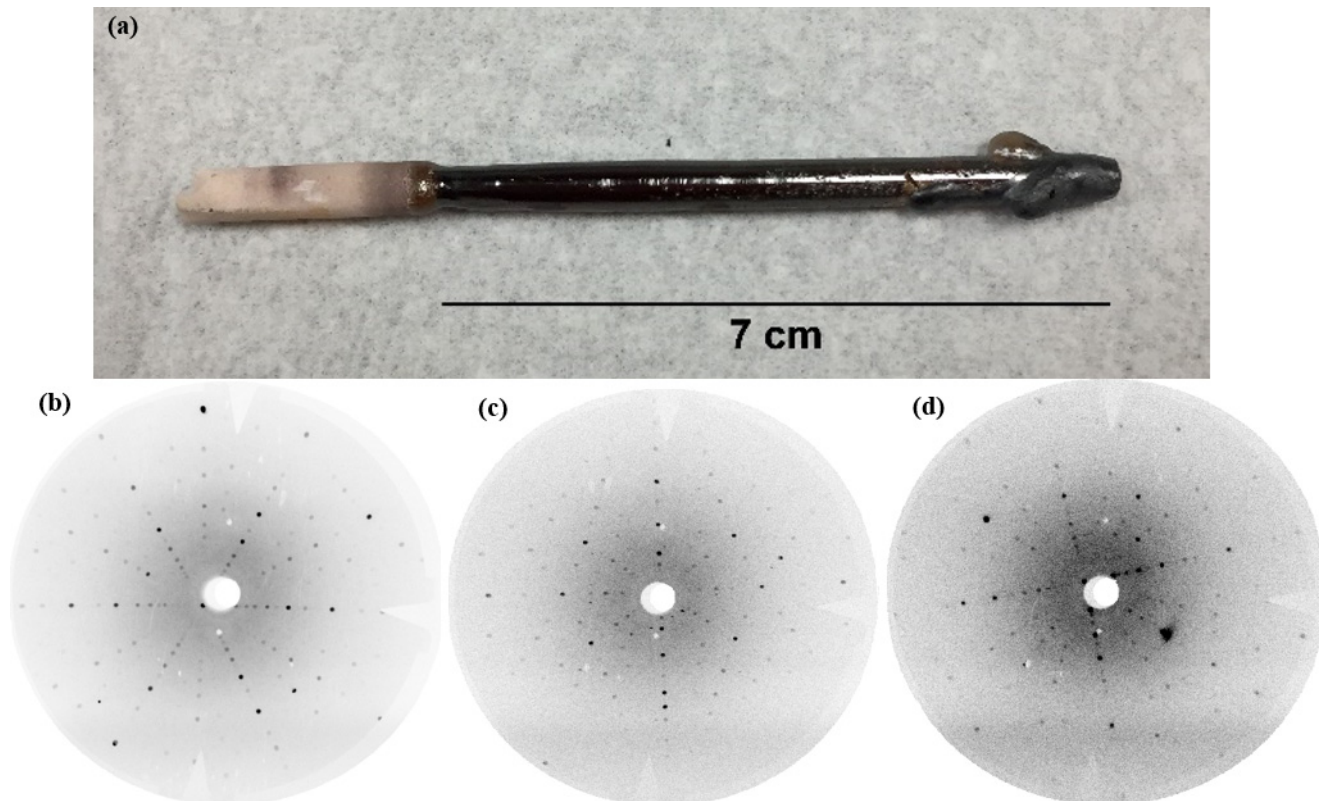


FIG. 2. (a) Resulting multicrystal of $(5RE_{0.2})_2\text{Ti}_2\text{O}_7$ of 7 cm length. (b)–(d) Laue diffraction patterns of $(5RE_{0.2})_2\text{Ti}_2\text{O}_7$ taken from various sections of the ingot showing good quality with (b) aligned in the [111], (c) in the [110], and (d) in the [100].

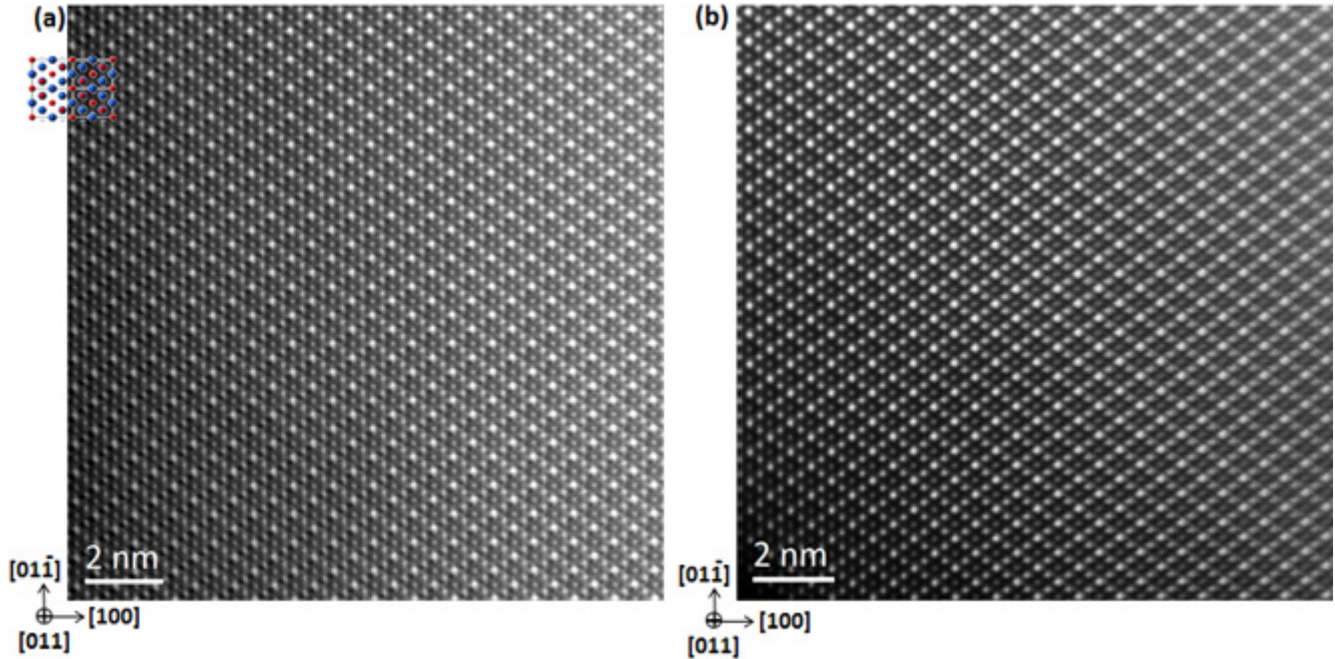


FIG. 3. Typical HAADF-STEM images along the $[011]$ zone axis for (a) single-crystalline and (b) polycrystalline $(5RE_{0.2})_2Ti_2O_7$, respectively. The inset in (a) is the crystal structure in this projection, where only cations are shown (the red and the blue are Ti and rare-earth atoms, respectively). The intensity variations arise from three types of atomic columns along this direction. The columns with brightest, intermediate, and weakest contrasts involve 100% rare-earth atoms, 50% rare-earth atoms plus 50% Ti atoms, and 100% Ti atoms, respectively.

polycrystalline and single-crystal samples. A comparison of the compositions and elemental percentages in specific areas of each sample is found in the Supplemental Material [41], along with chemical composition mapping of $(5RE_{0.2})_2Ti_2O_7$ polycrystal at $10\ \mu m$ (Fig. S4 in SM [41]), showing compositional uniformity of the five rare-earth cations at this scale.

Given the configurational complexity of this oxide, it is necessary to employ multiple microscopy methods to provide a better understanding of this material's structure and ion distribution at different scales. STEM-EELS was used to examine the homogeneity at smaller scales and further confirms a single-phase structure in both the single-crystal and polycrystalline materials. In what follows we discuss the nanoscale analysis for the single crystal. For further discussion of the polycrystal and atomic-scale homogeneity, please refer to the Supplemental Material [41].

As shown in the inset in Fig. 3(a), three types of cationic columns can be observed along the $[011]$ direction, which consist of 100% heavier rare-earth atoms, 50% rare-earth atoms plus 50% Ti atoms, and 100% lighter Ti atoms, respectively. Since the HAADF image intensity is roughly proportional to Z^2 (Z is the atomic number), these three types of columns show brightest, intermediate, and weakest contrasts, respectively. No obvious local structural imperfections were observed in the single-crystalline [Fig. 3(a)] and polycrystalline [Fig. 3(b)] samples, indicating the mixed occupation of the five rare-earth elements maintains the pyrochlore structure, consistent with the x-ray diffraction (XRD) result.

In contrast, as depicted in Fig. 4(a), along the $[001]$ direction each cationic column involves 50% rare-earth atoms plus 50% Ti atoms, suggesting an optimal zone axis for the uniformity analysis on the five rare-earth elements Yb, Tb, Gd, Dy, and Er in this pyrochlore structure. A region with in-plane dimensions of $27 \times 27\ nm$ for the single-crystalline sample [Fig. 4(a)] was selected to analyze the distribution of the five rare-earth elements at different scales. Using the log-ratio method as described in [42,43] from the corresponding low-loss EEL spectrum (Fig. S5a in the SM), the thickness for this region is calculated to be around 26 nm, i.e., 25 unit cells with 25 rare-earth atoms and 25 Ti atoms in each cationic column. The M_5 edges for these five rare-earth elements in the core-loss EEL spectra (Fig. S5b in SM) were used to acquire the chemical maps. Pixel sizes for the EEL mapping were first set to be around $0.7 \times 0.7\ nm$, i.e., containing information of ~ 200 rare-earth atoms for each pixel. The obtained maps using their M_5 edges are shown in Figs. 4(c)–4(g), respectively. These maps suggest a quite uniform distribution of these five rare-earth elements at such scale. Similar results were found for the polycrystalline sample using the same process described for the single crystal. It can be concluded from the STEM-EELS results that the five rare-earth cations in the $(5RE_{0.2})_2Ti_2O_7$ samples are distributed homogeneously down to $\sim 2.3\ nm$.

D. Magnetic properties

Figure 5 shows a comparison of the DC magnetic susceptibility measurements for polycrystalline and

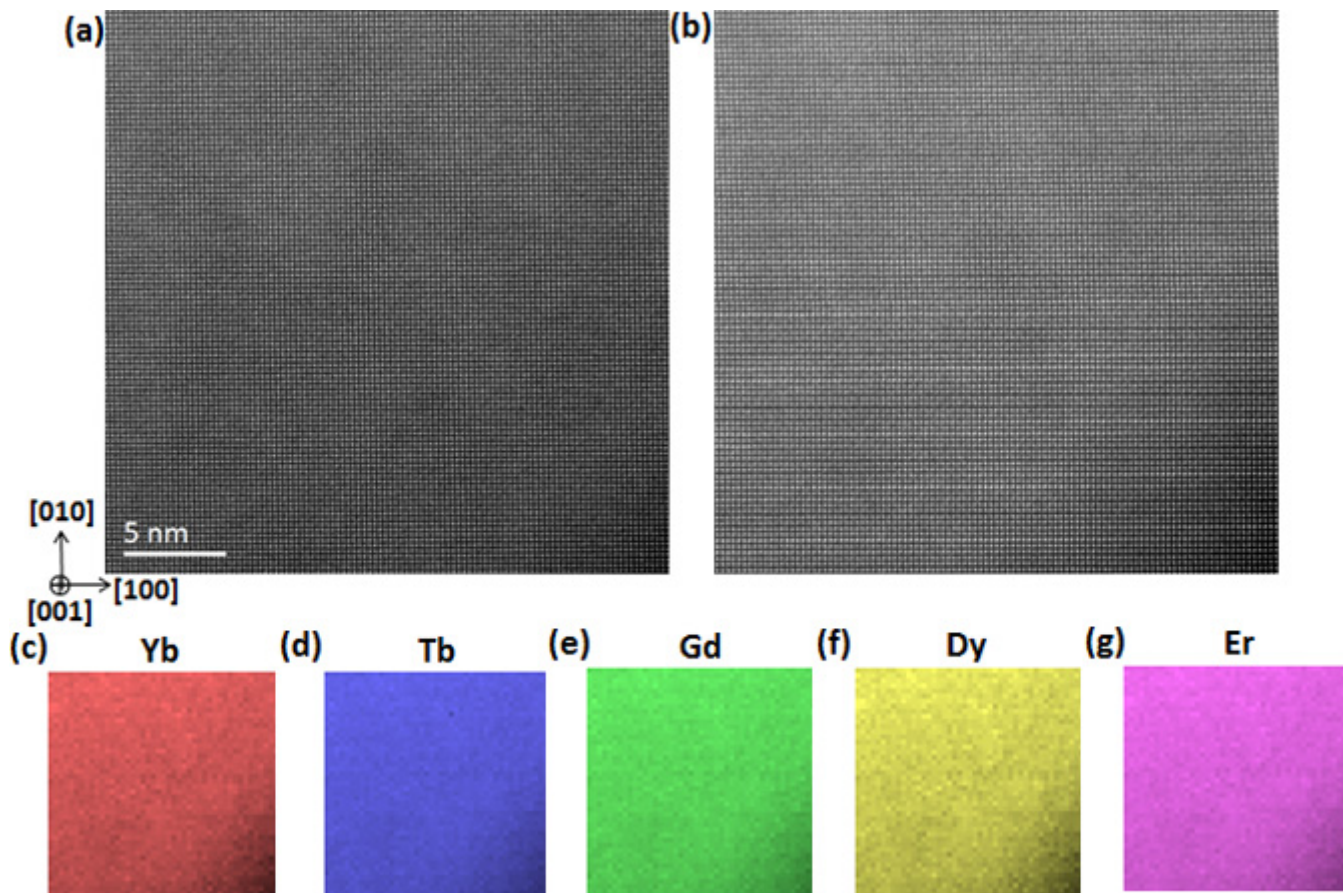


FIG. 4. HAADF-STEM imaging and nanoscale electron-energy loss spectroscopy (EELS) mapping along [001] for the single-crystalline $(SRE_{0.2})_2Ti_2O_7$. (a) Atomic-resolution HAADF image for the EELS mapping region with the dimension of 27×27 nm. (b)–(g) EELS mapping analysis: (b) HAADF image recorded simultaneously during the EELS data set acquisition; (c) Yb, (d) Tb, (e) Gd, (f) Dy, and (g) Er chemical maps obtained from their M_5 signals, respectively. Note that each pixel in the EELS maps is scanned by 16×16 for the simultaneously recorded HAADF image in (b), resulting in atomic resolution in (b) with nanoscale resolution in the EELS maps in (c)–(g).

single-crystalline $(SRE_{0.2})_2Ti_2O_7$. Both samples [Figs. 5(a) and 5(b)] show paramagnetic behavior from 3 to 300 K. Curie-Weiss temperatures and effective magnetic moments were determined for each sample using the Curie-Weiss fits of the inverse susceptibility and are also listed in Table II. The Curie-Weiss law, $\chi = \frac{C}{T - \theta_{CW}}$, was used for these Curie-Weiss fits where χ is the magnetic susceptibility, C is the

Curie constant, T is the absolute temperature, and θ_{CW} is the Curie-Weiss temperature [44]. Using linear fits between 50 and 300 K, the Curie-Weiss temperature for the single crystal is $\theta_{CW} = -13.06(6)$ K and for the polycrystal $\theta_{CW} = -2.91(6)$ K. These temperatures are both comparable to the Curie-Weiss temperatures found for the rare-earth titanate pyrochlores [44–52] and found in Table III.

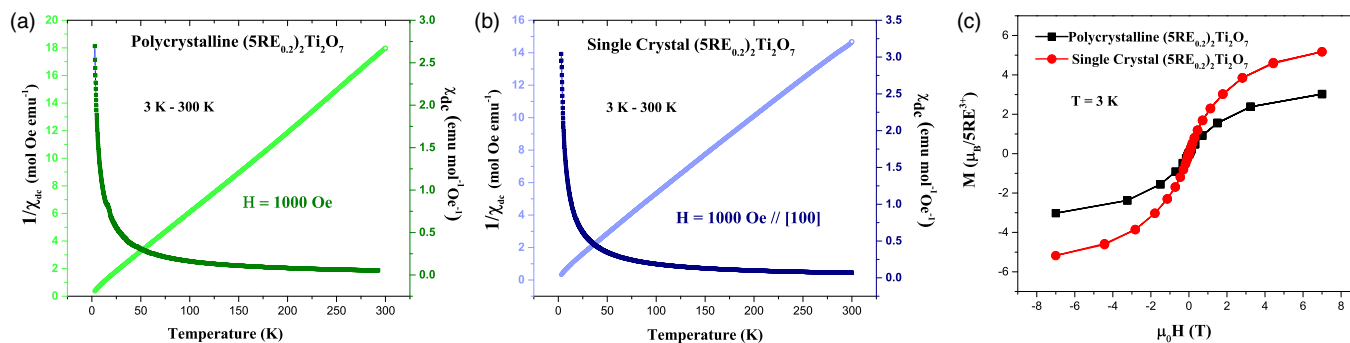


FIG. 5. DC susceptibility measurements on $(SRE_{0.2})_2Ti_2O_7$ polycrystal (a) and single crystal with applied magnetic field along the [100] direction (b) from 3 to 300 K, along with the magnetization curves (c) at 3 K from -7 to 7 T.

TABLE II. Calculated effective magnetic moments, applied field direction, temperature ranges, and Curie-Weiss temperatures for $(5RE_{0.2})_2Ti_2O_7$.

Sample	Field direction	Temperature range (K)	Magnetic moment (μ_B)	Curie-Weiss temperature (K)
Single crystal	along [100]	3–20	5.79	–2.98(0)
		50–300	6.50	–13.06(6)
Polycrystal	–	3–20	5.46	–3.14(1)
		50–300	5.87	–2.91(6)

*Estimated standard deviations are 1σ .

The single crystal's θ_{CW} is close to that of $Gd_2Ti_2O_7$ and $Er_2Ti_2O_7$, while the polycrystal's θ_{CW} falls in between those of $Gd_2Ti_2O_7$ and $Dy_2Ti_2O_7$. Since the Curie-Weiss temperatures for both samples are negative, antiferromagnetic frustration in the lattice and antiferromagnetic exchange coupling are expected. The discrepancy between the θ_{CW} temperatures of the single crystal and polycrystal is much reduced when using the Curie-Weiss fits between 3 and 20 K, with $\theta_{CW} = -2.98(0)$ K for the single crystal and $\theta_{CW} = -3.14(1)$ K for the polycrystal. For the single crystal, there are some minor changes in slope between the higher and lower temperature fit ranges. This could be an indication of crystal electric field effects causing fluctuation of the magnetic interactions at the different temperature ranges.

The effective magnetic moment from 50 to 300 K for the single crystal is $\mu_{\text{eff}} = 6.50 \mu_B$, making it slightly higher than the polycrystal's effective moment ($\mu_{\text{eff}} = 5.87 \mu_B$). From 3 to 20 K, the effective magnetic moments for the polycrystal ($\mu_{\text{eff}} = 5.46 \mu_B$) and single crystal ($\mu_{\text{eff}} = 5.79 \mu_B$) are more agreeable but remain consistent with the higher temperature calculated values. These values are smaller than the calculated average (roughly $\mu_{\text{eff}} = 8.48 \mu_B$) from the free-ion magnetic moments of each of the five rare-earth cations having an

oxidation state of 3+ listed in Table III. It is probable that competing magnetic interactions between the five different rare-earth cations on the A site due to some level of A-site cation disorder, chemical pressure, or possible lattice distortions could contribute to the overall smaller effective magnetic moments. The effective magnetic moments of the single-component rare-earth titanate pyrochlores found from literature [45–52] also show signs of variation compared to their expected free-ion magnetic moments. Due to single-ion magnetic anisotropy in $Er_2Ti_2O_7$ and $Dy_2Ti_2O_7$, the values reported for these compounds vary depending on field and direction [45,50,52]. Several studies have found smaller values for the effective magnetic moments in comparison to their free-ion moments [45–46,50–52], including a study that reported the effective magnetic moment of $Yb_2Ti_2O_7$ showing temperature dependence [45]. It is therefore difficult to fully determine an average of the single-component rare-earth pyrochlore oxides that agrees perfectly with the effective magnetic moments found for both the HEO polycrystal and single crystal.

The magnetization curves for the polycrystal and single-crystal samples obtained at 3 K are displayed in Fig. 5(c). Neither crystal nor polycrystal reaches complete magnetic

TABLE III. Compilation of literature-reported magnetic moments for the single-component rare-earth pyrochlore oxides, applied field direction (for single crystals), temperature ranges measured, free-ion magnetic moments, and Curie-Weiss temperatures^a.

Rare-earth ion	Sample	Field direction	Temperature range (K)	$RE_2^{3+}Ti_2O_7$ magnetic moment (μ_B)	Free-ion magnetic moment (μ_B) Ref. [44]	Curie-Weiss temperature (K)	Reference
Yb ³⁺	Polycrystal	–	5–11	3.33	4.54	0.59	[45]
	Polycrystal	–	–	1.15		0.75	[46]
Tb ³⁺	Polycrystal	–	–	9.40	9.72	–19	[47]
	Polycrystal	–	200–300	9.60		–18.9	[48]
Gd ³⁺	Polycrystal	–	50–300	7.22	7.94	–8.95	[45]
	Polycrystal	–	10–300	7.70		–9.60	[49]
	Polycrystal	–	–	7.80		–11.70	[51]
Er ³⁺	Polycrystal	–	50–300	8.93	9.58	–15.93	[45]
	Polycrystal	–	20–50	9.34		–22.3	
	Single crystal	Along $[1\bar{1}0]$	–	3.01		–	[52]
Dy ³⁺	Polycrystal	–	10–20	9.59	10.65	–0.20	[45]
	Polycrystal	–	–	9.96		–0.65	[51]
	Single crystal	Along (111) axis	Near 70 Near 300	10.03 10.51		–0.8 –	[50]

^a–" Indicates no reported value.

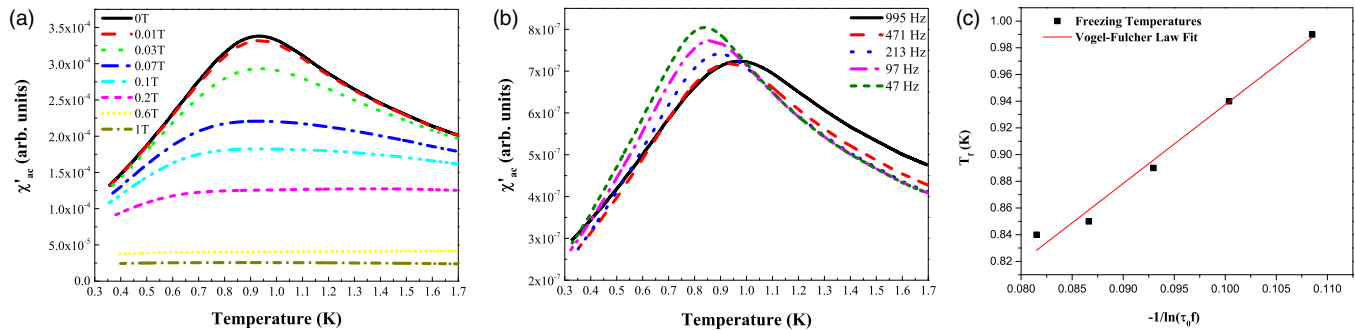


FIG. 6. AC susceptibility measurements (the real part) on single crystal $(5RE_{0.2})_2Ti_2O_7$ from temperatures of 0.3 to 1.7 K with (a) magnetic fields ranging from 0 to 1 T and (b) dependence on frequency ranging from 47 to 995 Hz, indicating a spin-glass magnetic ground state. (c) Linear relation of frequency dependence to freezing temperature (Vogel-Fulcher law).

saturation up to 7 T, and higher magnetic fields are needed to determine the saturation magnetization. The $(5RE_{0.2})_2Ti_2O_7$ single crystal shows a higher magnetization overall in comparison to the polycrystal.

AC susceptibility measurements on the single-crystal sample between 0.3 and 1.7 K are displayed in Fig. 6. A noticeable broad peak near 0.94 K in Fig. 6(a) begins to decrease and shift toward lower temperatures as the field is increased from 0 to 1 T, indicating that the system's interactions are antiferromagnetic. Figure 6(b) shows a peak that is characteristic of the spin-freezing temperature at approximately $T_f = 0.84$ K and moves from 0.84 to 0.98 K as the frequency increases from 47 to 995 Hz. This frequency dependence may signal a possible spin-glass ground state.

In order to have a spin-glass material, site disorder and frustration must be present [53]. As mentioned previously, disorder exists in this material due to the presence and randomization of the five rare-earth cations on the A site. The frustration index $f = -\frac{\theta_{CW}}{T_f}$ is often used to measure the level of frustration in a system and indicates frustration if $f > 1$ [53]. In $(5RE_{0.2})_2Ti_2O_7$, we find a frustration value of ~ 15.5 using the single-crystal values $\theta_{CW} = -13.06(6)$ K and $T_f = 0.84$ K. This value represents a material having strong geometric frustration ($f > 10$), providing evidence for a spin glass [53,54]. If the single-crystal value $\theta_{CW} = -2.98(0)$ K found from the Curie-Weiss fit between 3 and 20 K is used, we get a frustration value of ~ 3.5 , which is still a clear indicator of system frustration. Figure 6(c) is a relation of the frequency dependence with the freezing temperature using the Vogel-Fulcher law represented by $T_f = T_0 - \frac{E_a}{k_B \ln(\tau_0 f)}$, where E_a is the activation energy, τ_0 is the intrinsic relaxation time, f is the frequency, and T_0 is the ideal glass temperature for the system [54,55]. A τ_0 value between 1×10^{-13} s (conventional spin glasses) and 1×10^{-7} s (cluster glasses) represents the typical range of possible intrinsic relaxation times for spin glasses [53–55]. For this reason, 1×10^{-7} s is used for τ_0 in this fit and gave reasonable values of $E_a = 0.5$ meV and $T_0 = 0.37$ K. The fit shows reasonable linearity of the freezing temperatures using the Vogel-Fulcher law, providing extended evidence of glassy behavior. Although there is significant evidence for a spin-glass ground state, further measurements, such as specific heat and inelastic neutron

scattering, are still needed to verify this behavior, understand the local magnetic structure, and confirm the ground-state transition.

IV. CONCLUSION

We report the synthesis, structure, and magnetic characterization of a high-entropy, configurationally complex oxide $(Yb_{0.2}Tb_{0.2}Gd_{0.2}Dy_{0.2}Er_{0.2})_2Ti_2O_7$, also referred to as $(5RE_{0.2})_2Ti_2O_7$. We have shown that this material can be synthesized in the cubic pyrochlore phase (227), and single crystals of good quality can be grown using the floating-zone growth technique. STEM-EELS results further support single-phase polycrystalline and single-crystalline materials and confirm cation homogeneity down to ~ 2.3 nm. Susceptibility and magnetization studies on this oxide indicate antiferromagnetic exchange coupling, and the effective magnetic moments and Curie-Weiss temperatures were determined and reported. Low-temperature AC susceptibility measurements suggest a spin-glass magnetic ground state.

ACKNOWLEDGMENTS

D.M. acknowledges support from the Gordon and Betty Moore 385 Foundations EPIQS Initiative Grant No. GBMF9069. J.-Q.Y. acknowledges support from the U.S. Department of Energy (US DOE), Office of Science, Basic Energy Sciences, Materials Science and Engineering Division. H.D.Z. acknowledges support by the Department of Energy (DOE) under Award No. DE-SC-0020254. X.R.D. was performed at the Diffraction Facility of the Joint Institute for Advanced Materials (JIAM) at The University of Tennessee, Knoxville. The STEM work in this research was conducted at the ORNL's Center for Nanophase Materials Sciences (CNMS), which is a DOE Office of Science User Facility. A portion of this work was also performed at the National High Magnetic Field Laboratory, which is supported by the National Science Foundation through Cooperative Agreement No. DMR-1644779 and the State of Florida. We thank Dr. Michael Koehler, Dr. Deepak Sapkota, Dr. Ganesh Pokharel, and Dr. Zhiling Dun for their helpful discussions on the data presented in this report.

- [1] C. M. Rost, E. Sachet, T. Borman, A. Moballegh, E. Dickey, D. Hou, J. Jones, S. Curtarolo, and J.-P. Maria, Entropy-stabilized oxides, *Nat. Commun.* **6**, 8485 (2015).
- [2] A. Sarkar, L. Velasco, D. Wang, Q. Wang, G. Talasila, L. de Biasi, C. Kubel, T. Brezesinski, S. S. Bhattacharya, H. Hahn, and B. Breitung, High entropy oxides for reversible energy storage, *Nat. Commun.* **9**, 3400 (2018).
- [3] J. Zhang, J. Yan, S. Calder, Q. Zheng, M. McGuire, D. Abernathy, Y. Ren, S. Lapidus, K. Page, H. Zheng, J. Freeland, J. Budai, and R. Hermann, Long range antiferromagnetic order in a rocksalt high entropy oxide, *Chem. Mater.* **31**, 3705 (2019).
- [4] R. Djenadic, A. Sarkar, O. Clemens, C. Loho, M. Botros, V. Chakravadhanula, C. Kubel, S. S. Bhattacharya, A. Gandhi, and H. Hahn, Multicomponent equiatomic rare earth oxides, *Mater. Res. Lett.* **5**, 102 (2017).
- [5] J. Gild, M. Samiee, J. L. Braun, T. Harrington, H. Vega, P. E. Hopkins, K. Vecchio, and J. Luo, High-entropy fluorite oxides, *J. Eur. Ceram. Soc.* **38**, 3578 (2018).
- [6] S. Jiang, T. Hu, J. Gild, N. Zhou, J. Nie, M. Qin, T. Harrington, K. Vecchio, and J. Luo, A new class of high-entropy perovskite oxides, *Scr. Mater.* **142**, 116 (2018).
- [7] A. Sarkar, R. Djenadic, D. Wang, C. Hein, R. Kautenburger, O. Clemens, and H. Hahn, Rare earth and transition metal based entropy stabilised perovskite type oxides, *J. Eur. Ceram. Soc.* **38**, 2318 (2018).
- [8] R. Witte, A. Sarkar, R. Kruk, B. Eggert, R. A. Brand, H. Wende, and H. Hahn, High-entropy oxides: An emerging prospect for magnetic rare-earth transition metal perovskites, *Phys. Rev. Mater.* **3**, 034406 (2019).
- [9] Y. Sharma, B. L. Musico, X. Gao, C. Hua, A. F. May, A. Herklotz, A. Rastogi, D. Mandrus, J. Yan, H. N. Lee, M. F. Chisholm, V. Keppens, and T. Z. Ward, Single-crystal high entropy perovskite oxide epitaxial films, *Phys. Rev. Mater.* **2**, 060404 (2018).
- [10] J. Dabrowa, M. Stygar, A. Mikula, A. Knapik, K. Mroczka, W. Tejchman, M. Danielewski, and M. Martin, Synthesis and microstructure of the (Co, Cr, Fe, Mn, Ni)₃O₄ high entropy oxide characterized by spinel structure, *Mater. Lett.* **216**, 32 (2018).
- [11] B. L. Musico, Q. Wright, T. Z. Ward, A. Grutter, E. Arenholz, D. Gilbert, D. Mandrus, and V. Keppens, Tunable magnetic ordering through cation selection in entropic spinel oxides, *Phys. Rev. Mater.* **3**, 104416 (2019).
- [12] Y. Dong, K. Rena, Y. Lu, Q. Wang, J. Liu, and Y. Wang, High-entropy environmental barrier coating for the ceramic matrix composites, *J. Eur. Ceram. Soc.* **39**, 2574 (2019).
- [13] B. L. Musico, D. Gilbert, T. Z. Ward, K. Page, E. George, J. Yan, D. Mandrus, and V. Keppens, The emergent field of high entropy oxides: Design, prospects, challenges, and opportunities for tailoring material properties, *APL Mater.* **8**, 040912 (2020).
- [14] D. Bérardan, S. Franger, A. K. Meenab, and N. Dragoe, Room temperature lithium superionic conductivity in high entropy oxides, *J. Mater. Chem. A* **4**, 9536 (2016).
- [15] Z. Zhao, H. Xiang, F. Z. Dai, Z. Peng, and Y. Zhou, (La_{0.2}Ce_{0.2}Nd_{0.2}Sm_{0.2}Eu_{0.2})₂Zr₂O₇: A novel high-entropy ceramic with low thermal conductivity and sluggish grain growth rate, *J. Mater. Sci. Technol.* **35**, 2647 (2019).
- [16] F. Li, L. Zhou, J. X. Liu, Y. Liang, and G. J. Zhang, High-entropy pyrochlores with low thermal conductivity for thermal barrier coating materials, *J. Adv. Ceram.* **8**, 576 (2019).
- [17] D. B. Miracle and O. N. Senkov, A critical review of high entropy alloys and related concepts, *Acta Mater.* **122**, 448 (2017).
- [18] J. W. Yeh, S. K. Chen, S. J. Lin, J. Y. Gan, T. S. Chin, T. T. Shun, C. H. Tsau, and S. Y. Chang, Nanostructured high-entropy alloys with multiple principal elements: Novel alloy design concepts and outcomes, *Adv. Eng. Mater.* **6**, 299 (2004).
- [19] J. Zhang, J. Lian, A. Fuentes, F. Zhang, M. Lang, F. Lu, and R. C. Ewing, Enhanced radiation resistance of nanocrystalline pyrochlore Gd₂(Ti_{0.65}Zr_{0.35})₂O₇, *Appl. Phys. Lett.* **94**, 243110 (2019).
- [20] R. C. Ewing, W. J. Weber, and J. Lian, Nuclear waste disposal-pyrochlore (A₂B₂O₇): Nuclear waste form for the immobilization of plutonium and “minor” actinides, *J. Appl. Phys.* **95**, 5949 (2004).
- [21] L. Yang, C. Zhu, Y. Sheng, H. Nian, Q. Li, P. Song, W. Lu, J. Yang, and B. Liu, Investigation of mechanical and thermal properties of rare earth pyrochlore oxides by first-principles calculations, *J. Am. Ceram. Soc.* **102**, 2830 (2019).
- [22] J. Lian, J. Chen, L. M. Wang, and R. C. Ewing, Radiation-induced amorphization of rare-earth titanate pyrochlores, *Phys. Rev. B* **68**, 134107 (2003).
- [23] D. Yang, Y. Xia, J. Wen, J. Liang, P. Mu, Z. Wang, Y. Li, and Y. Wang, Role of ion species in radiation effects of Lu₂Ti₂O₇ pyrochlore, *J. Alloys Compd.* **693**, 565 (2017).
- [24] H. Zhou and C. R. Wiebe, High-pressure routes to new pyrochlores and novel magnetism, *Inorganics* **7**, 49 (2019).
- [25] C. R. Wiebe and A. M. Hallas, Frustration under pressure: Exotic magnetism in new pyrochlore oxides, *APL Mater.* **3**, 041519 (2015).
- [26] I. A. Ryzhkin, Magnetic relaxation in rare-earth oxide pyrochlores, *J. Exp. Theor. Phys.* **101**, 481 (2005).
- [27] M. P. van Dijk, A. J. Burggraaf, A. N. Cormack, and C. R. A. Catlow, Defect structures and migration mechanisms in oxide pyrochlores, *Solid State Ionics* **17**, 159 (1985).
- [28] G. Lan, B. Ouyang, and J. Song, The role of low-lying optical phonons in lattice thermal conductance of rare-earth pyrochlores: A first-principle study, *Acta Mater.* **91**, 304 (2015).
- [29] J. S. Gardner, M. J. P. Gingras, and J. E. Greedan, Magnetic pyrochlore oxides, *Rev. Mod. Phys.* **82**, 53 (2010).
- [30] J. E. Greedan, Frustrated rare earth magnetism: Spin glasses, spin liquids and spin ices in pyrochlore oxides, *J. Alloys Compd.* **408–412**, 444 (2006).
- [31] J. G. Rau and M. J. Gingras, Frustrated quantum rare-earth pyrochlores, *Annu. Rev. Condens. Matter Phys.* **10**, 357 (2019).
- [32] M. A. Subramanian, G. Aravamudan, and G. V. Subba Rao, Oxide pyrochlores—A review, *Prog. Solid State Chem.* **15**, 55 (1983).
- [33] H. W. J. Blöte, R. F. Wielinga, and W. J. Huiskamp, Heat-capacity measurements on rare-earth double oxides R₂M₂O₇, *Physica* **43**, 549 (1969).
- [34] A. V. Shlyakhtina, P. Fedtke, A. Busch, I. V. Kolbanev, T. Barfels, M. Wienecke, A. E. Sokolov, V. A. Ulianov, V. A. Trounov, and L. G. Shcherbakova, Effect of Ca-doping on the electrical conductivity of oxide ion conductor Yb₂Ti₂O₇, *Solid State Ionics*, **179**, 1004 (2008).
- [35] A. J. Princep, H. C. Walker, D. T. Adroja, D. Prabhakaran, and A. T. Boothroyd, Crystal field states of Tb³⁺ in the pyrochlore spin liquid Tb₂Ti₂O₇ from neutron spectroscopy, *Phys. Rev. B* **91**, 224430 (2015).

- [36] A. Garbout, I. Ben Taazayet-Belgacem, and M. Ferid, Structural, FTIR, XRD and Raman scattering of new rare-earth titanate pyrochlore-type oxides $\text{Ln EuTi}_2\text{O}_7$ ($\text{Ln} = \text{Gd}, \text{Dy}$), *J. Alloys Compd.* **573**, 43 (2013).
- [37] O. Knop, F. Brisse, and L. Castelliz, Pyrochlores V. Thermoanalytic, X-ray, neutron, infrared, and dielectric studies of $\text{A}_2\text{Ti}_2\text{O}_7$ titanates, *Can. J. Chem.* **47**, 971 (1969).
- [38] A. R. Heredia, M. Quintana Garcia, J. L. Perez Mazariego, and R. Escamilla, X-ray diffraction and Raman spectroscopy on $\text{Gd}_2(\text{Ti}_{2-y}\text{Te}_y)\text{O}_7$ prepared at high pressure and high temperature, *J. Alloys Compd.* **504**, 446 (2010).
- [39] Q. J. Li, L. M. Xu, C. Fan, F. B. Zhang, Y. Y. Lv, B. Ni, Z. Y. Zhao, and X. F. Sun, Single crystal growth of the pyrochlores $\text{R}_2\text{Ti}_2\text{O}_7$ ($\text{R} = \text{rare earth}$) by the optical floating-zone method, *J. Cryst. Growth.* **377**, 96 (2013).
- [40] B. H. Toby and R. B. Von Dreele, GSAS-II: The genesis of a modern open-source all purpose crystallography software package, *J. Appl. Crystallogr.* **46**, 544 (2013).
- [41] See Supplemental Material at <http://link.aps.org/supplemental/10.1103/PhysRevMaterials.4.104411> for the table of the Rietveld refinement crystallographic parameters, XRD pattern comparison of the single-crystal and polycrystal, scanning electron microscopy (SEM) and energy-dispersive x-ray (EDX) data, color-mapping of the polycrystal, the remaining STEM results for the polycrystal and single crystal (nanoscale and atomic scales), and additional magnetic susceptibility data.
- [42] T. Malis, S. C. Cheng, and R. F. Egerton, EELS log-ratio technique for specimen-thickness measurement in the TEM, *J. Electron Microsc. Technol.* **8**, 193 (1988).
- [43] R. F. Egerton, Electron energy-loss spectroscopy in the TEM, *Rep. Prog. Phys.* **72**, 016502 (2009).
- [44] N. Spaldin, *Magnetic Materials: Fundamentals and Applications* (Cambridge University Press, Cambridge, 2011).
- [45] S. T. Bramwell, M. N. Field, M. J. Harris, and I. P. Parkin, Bulk magnetization of the heavy rare earth titanate pyrochlores – A series of model frustrated magnets, *J. Phys.: Condens. Matter.* **12**, 483 (1999).
- [46] J. A. Hodges, P. Bonville, A. Forget, A. Yaouanc, P. Dalmás de Reotier, G. Andre, M. Rams, K. Krolas, C. Ritter, P. C. M. Gubbens, C. T. Kaiser, P. J. C. King, and C. Baines, First-Order Transition in the Spin Dynamics of Geometrically Frustrated $\text{Yb}_2\text{Ti}_2\text{O}_7$, *Phys. Rev. Lett.* **88**, 077204 (2002).
- [47] J. S. Gardner, S. R. Dunsiger, B. D. Gaulin, M. J. P. Gingras, J. E. Greedan, R. F. Kiefl, M. D. Lumsden, W. A. MacFarlane, N. P. Raju, J. E. Sonier, I. Swainson, and Z. Tun, Cooperative Paramagnetism in the Geometrically Frustrated Pyrochlore Antiferromagnet $\text{Tb}_2\text{Ti}_2\text{O}_7$, *Phys. Rev. Lett.* **82**, 1012 (1999).
- [48] M. J. P. Gingras, B. C. denHertog, M. Faucher, J. S. Gardner, S. R. Dunsiger, L. J. Chang, B. D. Gaulin, N. P. Raju, and J. E. Greedan, Thermodynamic and single-ion properties of Tb^{3+} within the collective paramagnetic-spin liquid state of the frustrated pyrochlore antiferromagnet $\text{Tb}_2\text{Ti}_2\text{O}_7$, *Phys. Rev. B.* **62**, 6496 (2000).
- [49] N. P. Raju, M. Dion, M. J. P. Gingras, T. E. Mason, and J. E. Greedan, Transition to long-range magnetic order in the highly frustrated insulating pyrochlore antiferromagnet $\text{Gd}_2\text{Ti}_2\text{O}_7$, *Phys. Rev. B.* **59**, 14489 (1999).
- [50] Y. M. Jana, A. Sengupta, and D. Ghosh, Estimation of single ion anisotropy in pyrochlore $\text{Dy}_2\text{Ti}_2\text{O}_7$, a geometrically frustrated system, using crystal field theory, *J. Magn. Magn. Mater.* **248**, 7 (2002).
- [51] J. D. Cashion, A. H. Cooke, M. J. M. Leask, T. L. Thorp, and M. R. Wells, Crystal growth and magnetic susceptibility of some rare-earth compounds, *J. Mater. Sci.* **3**, 402 (1968).
- [52] J. D. M. Champion, M. J. Harris, P. C. W. Holdsworth, A. S. Wills, G. Balakrishnan, S. T. Bramwell, E. Cizmar, T. Fennell, J. S. Gardner, J. Lago, D. F. McMorrow, M. Orendac, A. Orendacova, D. McK. Paul, R. I. Smith, M. T. F. Telling, and A. Wildes, ErTiO : Evidence of quantum order by disorder in a frustrated antiferromagnet, *Phys. Rev. B.* **68**, 020401 (2003).
- [53] A. P. Ramirez, Strongly geometrically frustrated magnets, *Annu. Rev. Mater. Sci.* **24**, 453 (1994).
- [54] J. A. Mydosh and I. Ebrary, *Spin Glasses: An Experimental Introduction* (Taylor & Francis, London, 1993).
- [55] J. W. Krizan and R. J. Cava, NaCaCoF : A single crystal high-temperature pyrochlore antiferromagnet, *Phys. Rev. B.* **89**, 214401 (2014).